Applied Surface Science 755 (2027) 168810

Contents lists available at ScienceDirect

Applied Surface Science

journal homepage: www.elsevier.com/locate/apsusc

Full Length Article

# $Ti_3C_2T_x$ MXene-derived quantum dots with mixed terminations for humidity sensing: experimental studies and theoretical investigation via DFT

Yotsarayuth Seekaew [a], Weeraphat Pon-On [b], Pakpoom Reunchan [b], Audomsak Sripothongnack [b], Chatchawal Wongchoosuk [b,*]

[a] Department of Physics, Faculty of Science, Ramkhamhaeng University, Bang Kapi, Bangkok 10240, Thailand
[b] Department of Physics, Faculty of Science, Kasetsart University, Chatuchak, Bangkok 10900, Thailand

ARTICLE INFO

*Keywords:*
$Ti_3C_2T_x$ MXene
Humidity sensor
Quantum dots
DFT
Surface-termination vacancies

ABSTRACT

$Ti_3C_2T_x$ MXene quantum dots (QDs) with mixed surface terminations were synthesized via a top-down solvothermal method and applied as a high-performance resistive-type humidity sensor, supported by density functional theory (DFT) analysis. The $Ti_3C_2T_X$ MXene QDs (~ 3.4 nm) humidity sensor exhibit excellent sensing performance over 10–95% RH at room temperature, demonstrating high response, high sensitivity (269.4 kΩ/% RH), low hysteresis (< 0.86%), good repeatability and good long-term stability. The sensing mechanism involves charge transfer upon water adsorption and proton conduction through hydrogen-bonded networks via the Grotthuss mechanism. DFT calculations on O-, OH–, and F-terminated $Ti_3C_2T_x$ models indicate that termination-vacancy sites generally enhance $H_2O$ adsorption and charge redistribution compared with the corresponding vacancy-free surfaces. These results demonstrate the combined roles of nanoscale dimensions, mixed surface terminations, and vacancy-related adsorption sites in the humidity-sensing behavior of $Ti_3C_2T_x$ MXene QDs as promising materials for advanced humidity sensing applications.

## 1. Introduction

Humidity monitoring is important for environmental control, industrial processes, healthcare, and wearable electronics. Recent humidity sensors have employed resistive, capacitive, and electrochemical principles using various sensing materials with increasing attention to flexible and self-powered platforms [1–6]. For example, high-performance systems based on paper substrates [1], cellulose nanocrystal/NaCl [3], LiCl/carbon ink [4], proton-conducting polyaniline [5], and ionic liquids [6] have demonstrated broad RH detection ranges, rapid response, and low-power operation. Despite these advances, the development of humidity-sensitive materials with strong water adsorption, efficient charge transport, and tunable surface chemistry remains highly desirable. For this reason, MXene has emerged as a promising sensing material because of its high electrical conductivity, hydrophilic surface, and abundant surface terminations.

MXenes are a family of two-dimensional (2D) transition metal carbides and nitrides derived from layered MAX phases with the general formula $M_{n+1}AX_n$, where M represents an early transition metal, A is an A-group element from groups III A or IV A, and X is carbon and/or nitrogen. MXenes are synthesized via the selective etching of the A-layer from the parent MAX phase, producing $M_{n+1}AX_nT_x$ structures, where $T_x$ represents surface functional groups such as −O, –OH, and −F that are introduced during the chemical etching process [7,8]. Among the various MXene compositions, titanium carbide ($Ti_3C_2T_x$) has been the most extensively studied owing to its relatively simple synthesis, high electrical conductivity, hydrophilic surface chemistry, and excellent structural stability [9–11]. $Ti_3C_2T_x$ MXene is typically synthesized through the selective chemical etching of aluminum from the MAX phase $Ti_3AlC_2$ using hydrofluoric acid (HF) or fluoride-containing acidic solutions, followed by delamination to produce few-layer or single-layer nanosheets [12,13]. The resulting 2D $Ti_3C_2T_x$ MXene exhibits metallic conductivity, a high specific surface area, and abundant surface functional groups, which are beneficial for various electrochemical and sensing applications [14,15].

Recently, the dimensional reduction of 2D $Ti_3C_2T_x$ MXene nanosheets into zero-dimensional $Ti_3C_2T_x$ MXene quantum dots ($Ti_3C_2T_x$ MXene QDs) has emerged as an effective strategy to further enhance

* Corresponding author.
*E-mail address:* chatchawal.w@ku.ac.th (C. Wongchoosuk).

https://doi.org/10.1016/j.apsusc.2026.168810
Received 27 June 2026; Received in revised form 15 October 2026; Accepted 27 October 2026
Available online 28 October 2026
0169-4332/© 2026 Elsevier B.V. All rights are reserved, including those for text and data mining, AI training, and similar technologies.

their sensing performance. $Ti_3C_2T_x$ MXene QDs have been synthesized using various methods including hydrothermal treatment [16,17], solvothermal [18], ultrasonic exfoliation [19], chemical oxidation [20], and electrochemical exfoliation of $Ti_3C_2T_x$ MXene nanosheets [21], resulting in nanometer-sized particles typically ranging from 2 to 10 nm. These top-down methods allow the formation of ultra-small quantum dots with good dispersibility and abundant functional groups on their surfaces. The resulting $Ti_3C_2T_x$ MXene QDs exhibit quantum confinement effects, improved dispersibility, and a higher density of surface defects compared with their parent nanosheets [22]. Because of these advantages, $Ti_3C_2T_x$ MXene QDs have been widely investigated for chemical, biological, and sensing applications. For example, amino-functionalized $Ti_3C_2T_x$ MXene QDs have been utilized as fluorescent probes for detecting histidine in human serum through photoluminescence quenching mechanisms, demonstrating their potential in biomedical sensing [23]. In addition to biosensing, $Ti_3C_2T_x$ MXene QDs have also shown excellent performance in environmental and food safety monitoring. For instance, $Ti_3C_2T_x$ MXene QDs have been used as fluorescence probes for the detection of quercetin in food samples, where fluorescence quenching mechanisms enable highly sensitive and selective detection with detection limits in the nanomolar range [16]. For humidity sensing applications, $Ti_3C_2T_x$ MXene QDs have not yet been reported for humidity detection. To date, research has primarily focused on $Ti_3C_2T_x$ MXene nanosheets combined with other nanomaterials to further enhance sensing performance. For example, $Ti_3C_2T_x$ MXene integrated with semiconductors, such as $SnS_2$ [24], ZnS [25], CuO [26], and $SnO_2$ [27], can form heterojunctions that facilitate efficient charge separation and enhance sensing performance. Although $Ti_3C_2T_x$ MXene, MXene/polymer composites and MXene-based heterostructures have been extensively investigated for humidity sensing, the response of layered $Ti_3C_2T_x$ can be strongly influenced by water intercalation, interlayer swelling, and interflake charge transport [28–30]. Reducing $Ti_3C_2T_x$ to the ultrasmall quantum-dot scale increases the relative proportion of accessible surface and edge sites, which can provide additional adsorption sites for water molecules [22]. In addition to experimental studies, theoretical investigations based on density functional theory (DFT) have provided important insights into the gas-sensing behavior of $Ti_3C_2$ MXene nanosheets [31]. Computational studies have demonstrated that gas molecules such as CO, $COCl_2$, $NH_3$, $H_2S$, and $NO_2$ can absorb onto the pristine $Ti_3C_2$ MXene surfaces with appreciable adsorption energies, resulting in modifications to the electronic structure and work function. Therefore, $Ti_3C_2T_x$ MXene QDs represent a promising research direction for studying the performance of humidity sensing through both experimental and theoretical investigations.

In this work, $Ti_3C_2T_x$ MXene QDs were synthesized from $Ti_3C_2T_x$ MXene nanosheets via a top-down solvothermal method and subsequently used to fabricate a humidity sensor through a simple fabrication process. The synthesized $Ti_3C_2T_x$ MXene QDs exhibited mixed −O/–OH/-F surface terminations. Their structural characteristics and humidity sensing performance of the $Ti_3C_2T_x$ MXene QDs were systematically investigated. The fabricated $Ti_3C_2T_x$ MXene QDs-based humidity sensor demonstrated high response, excellent repeatability, and good stability over a wide relative humidity (RH) range of 10–95%. The humidity sensing mechanism was mainly attributed to charge transfer processes and the Grotthuss chain reaction. The DFT calculation was also performed to investigate the interactions between water molecules and the mixed −O/–OH/-F surface terminations of the $Ti_3C_2T_x$ MXene QDs.

## 2. Experiment details

### 2.1. Synthesis and fabrication of $Ti_3C_2T_x$ MXene QDs humidity sensor

The $Ti_3C_2T_x$ MXene (multilayer nanoflakes) was purchased from ACS Material, LLC. First, 40 mg of $Ti_3C_2T_x$ powder dispersed in 10 mL of nitric acid (5 M), which was then put in an oil bath and reacted at a constant temperature of 100ºC for 24 h. After cooling to room temperature, the solution was poured into 30 mL of ice water, and the pH of the solution was adjusted to 7 using NaOH (1 M). After centrifugation, the obtained sediment was redispersed in 40 mL of ultrapure water to obtain $Ti_3C_2T_x$ solution. The fabrication process of the $Ti_3C_2T_x$ MXene QDs sensor is illustrated in Fig. 1b. Interdigitated aluminum (Al) electrode patterns were deposited on an alumina sheet substrate ($4 \times 4$ mm$^2$) with an interdigit spacing of 100 μm using conventional photolithography, radio-frequency sputtering, and lift-off processes. Subsequently, 10 μL of the prepared $Ti_3C_2T_x$ MXene QDs suspension was deposited onto the Al interdigitated electrodes/alumina substrate (as shown in Fig. 1b) using a simple drop-coating method and then dried at room temperature.

### 2.2. Characterization and measurement of $Ti_3C_2T_x$ MXene QDs humidity sensor

The crystal structure of the samples was analyzed using an X-ray diffractometer (XRD, Bruker D8 Advance) with Cu Kα radiation ($\lambda = 1.5406$ Å). Field-emission transmission electron microscopy (FE-TEM, JEOL JEM-3100F) was employed to characterize morphology and elemental distribution. X-ray photoelectron spectroscopy (XPS, Axis Ultra DLD) was used to examine the chemical bonding and electronic states at the surface of the $Ti_3C_2T_x$ MXene QDs. The humidity-sensing performance of the $Ti_3C_2T_x$ MXene QDs sensor embedded in a custom-designed 250 mL chamber were evaluated using a standard flow-through system at room temperature ($26 \pm 2$ °C) and relative humidity (RH) ranging from 10% to 95%. Water vapor was generated by bubbling dry air through deionized (DI) water to serve as the humidity source. The desired RH levels were controlled by adjusting two mass flow controllers (MFCs) with the total flow rate maintained at 1000 sccm. A commercial temperature and humidity sensor (SHT15) was placed inside the 250 mL chamber to verify the RH and temperature values. For dynamic response measurements, dry air was first introduced into the chamber for 3 min to establish the baseline resistance of the sensor. Subsequently, humidified air from the bubbling system was introduced into the chamber for 3 min for humidity-sensing tests. The sensor resistance was monitored using a simple voltage divider circuit (applied voltage of 10 V) and recorded every 1 s via a custom LabVIEW program connected to a USB DAQ device (NI USB-6008). The response and recovery times of the $Ti_3C_2T_x$ MXene QDs humidity sensor are defined as the times required to reach 90% of the total resistance change during the adsorption process from 10% to 95% RH and the desorption process from 95% to 10% RH, respectively. The humidity response (S, (%)) of the sensor was calculated using the following equation: $S\ (\%) = ((R_{10\%\ RH} - R_{X\%\ RH})/R_{10\%\ RH}) \times 100$, where $R_{X\%\ RH}$ and $R_{10\%\ RH}$ represent the sensor resistance under humidified and the baseline humidity condition of 10% RH, respectively. Resistive humidity-sensor responses are commonly expressed using resistance ratios ($R/R_0$) or ($R_0/R$) or normalized relative resistance changes ($\Delta R/R_0$) [32]. In this work, the sensor resistance decreases monotonically with increasing RH. Therefore, the response definition used in this study was selected to represent the percentage decrease in resistance relative to the baseline resistance at 10% RH, thereby yielding a positive response value that increases with increasing humidity.

### 2.3. Computational method

All calculations were performed using the Vienna *ab initio* Simulation Package (VASP) [33,34]. The exchange–correlation interaction was described using the Perdew-Burke-Ernzerhof (PBE) functional within the generalized gradient approximation (GGA) [35]. Long-range van der Waals interactions were included using the Grimme DFT-D3 dispersion correction [36,37], which is widely used to provide a reliable description of interactions between small molecules and material surfaces [38,39]. A vacuum gap of 20 Å was introduced along the *z*-direction to

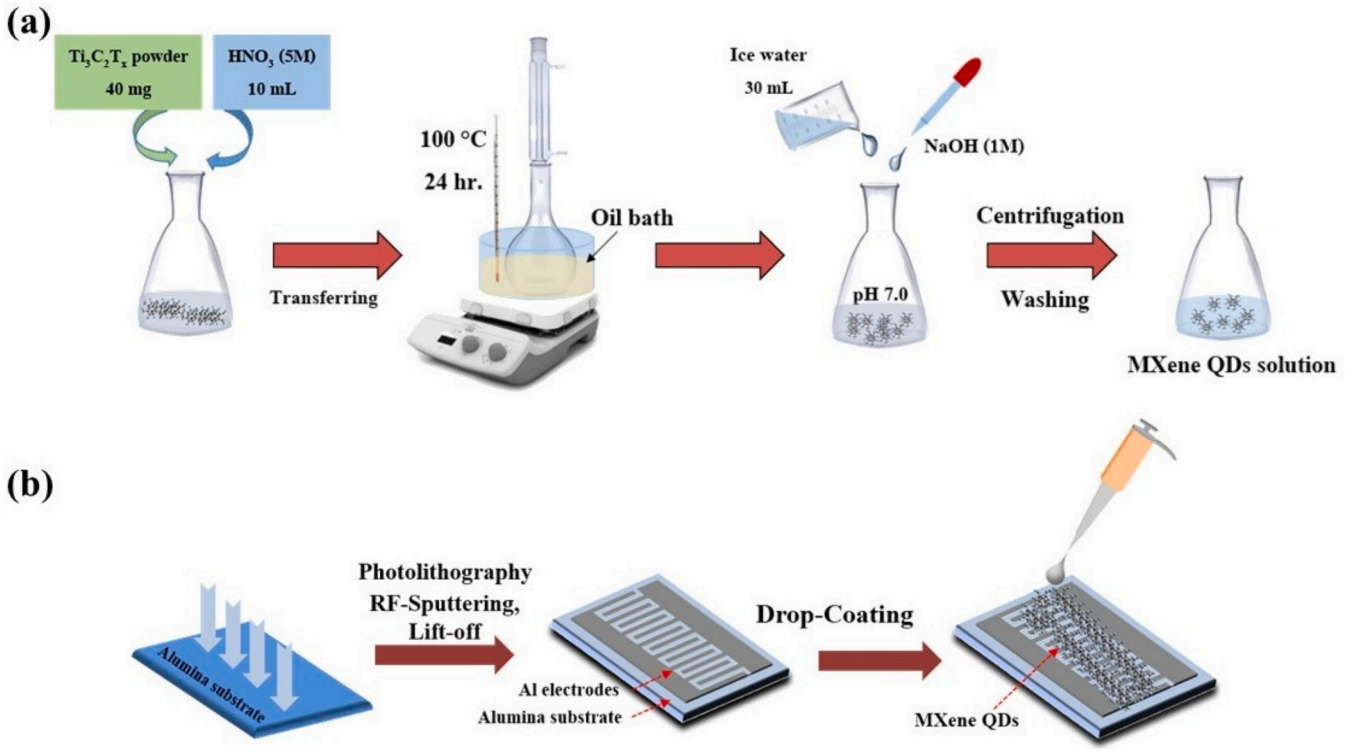



**Fig. 1.** Schematic diagrams of (a) the synthesis and (b) the fabrication processes of the $Ti_3C_2T_x$ MXene QDs humidity sensor.

avoid interactions between periodic images. The plane-wave cutoff energy was set to 520 eV, and the energy and force convergence criteria were $10^{-5}$ eV and 0.02 eV $Å^{-1}$, respectively. A 3 × 3 × 1 supercell was used for the $H_2O$ adsorption calculations, with Brillouin zone sampling performed using a Monkhorst-Pack 3 × 3 × 1 k-point mesh.

The adsorption energy was calculated using

$$E_{ads} = E_{tot}(Ti_3C_2T_x\text{-}H_2O) - E_{tot}(Ti_3C_2T_x) - E_{tot}(H_2O) \quad (1)$$

where $E_{tot}(Ti_3C_2T_x)$ and $E_{tot}(Ti_3C_2T_x\text{-}H_2O)$ are the total energy of the pristine or defective $Ti_3C_2T_2$ before and after absorbing a $H_2O$ molecule. $E_{tot}(H_2O)$ is the energy of an isolated $H_2O$ molecule.

## 3. Results and discussion

### 3.1. Morphological and compositional characterization

The XRD patterns of $Ti_3C_2T_x$ MXene QDs and $Ti_3C_2T_x$ MXene are shown in Fig. 2. The XRD pattern of $Ti_3C_2T_x$ MXene (JCPDS No. 52–0875) shows peaks at 2θ = 9.0°, 18.3°, 28.1°, 34.0°, 41.6°, and 60.5°

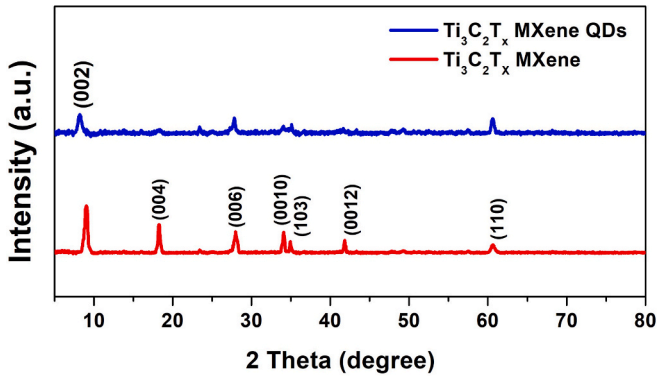



**Fig. 2.** XRD patterns of $Ti_3C_2T_x$ MXene QDs and $Ti_3C_2T_x$ MXene.

which correspond to the (002), (004), (006), (0010), (0012), and (110) planes of the 2D layered structure of $Ti_3C_2T_x$ MXene, respectively [11]. For $Ti_3C_2T_x$ MXene QDs, the (002) plane shifts to a lower angle of approximately 8.1°, broadens slightly, and decreases in intensity [23]. This change likely results from enhanced solvent intercalation between delaminated layers and heat treatment during synthesis [40].

The morphology and size of the as-prepared $Ti_3C_2T_x$ MXene QDs were investigated using FE-TEM as shown in Fig. 3. The TEM image (Fig. 3a) reveals the formation of uniform, quasi-spherical nanoparticles. The high-resolution TEM images presented in Fig. 3b and c demonstrate lattice fringes of the $Ti_3C_2T_x$ MXene QDs. The HRTEM image (Fig. 3c) showed lattice fringes of approximately 0.21 nm, corresponding to the (0110) facet of the $Ti_3C_2$ MXene [21]. The particle size distribution of the $Ti_3C_2T_x$ MXene QDs was determined from FE-TEM images using ImageJ software. Gaussian fitting of the particle size distribution histogram (Fig. 3d and Fig. S1 of Supporting Information) yields an average diameter of approximately 3.38 ± 0.39 nm, confirming their nanoscale dimensions within the quantum-dot-size regime. Furthermore, EDX was employed to determine the elemental composition of $Ti_3C_2T_x$ MXene QDs as shown in Fig. 3e. The weight percentages of the main elements are 14.49% titanium (Ti), 69.34% carbon (C), 2.56% F, and 13.61% oxygen (O). It should be noted that the weight percentage of carbon is higher than that of the other elements, which can be attributed to the carbon film on the copper TEM grid used during EDX analysis.

The XPS survey spectra of the $Ti_3C_2T_x$ MXene QDs show four characteristic peaks corresponding to the constituent elements C 1s, Ti 2p, O 1s, and F 1s as shown in Fig. 4a. In Fig. 4b, the C 1s core-level spectrum shows peaks at 285.1, 286.5, and 288.5 eV, which are assigned to C–C, C-O, and C-O/O-C=O carbon bonds, respectively [41–43]. The component at 285.1 eV is mainly associated with graphitic, aliphatic, or adventitious carbon, whereas the higher binding energy of components are attributed predominantly to oxygen-containing carbon species formed during the $HNO_3$-assisted treatment. Notably, a clearly resolved low-binding-energy carbide–carbon component, typically associated with C-Ti bonding in $Ti_3C_2T_x$, is not observed. This suggests substantial

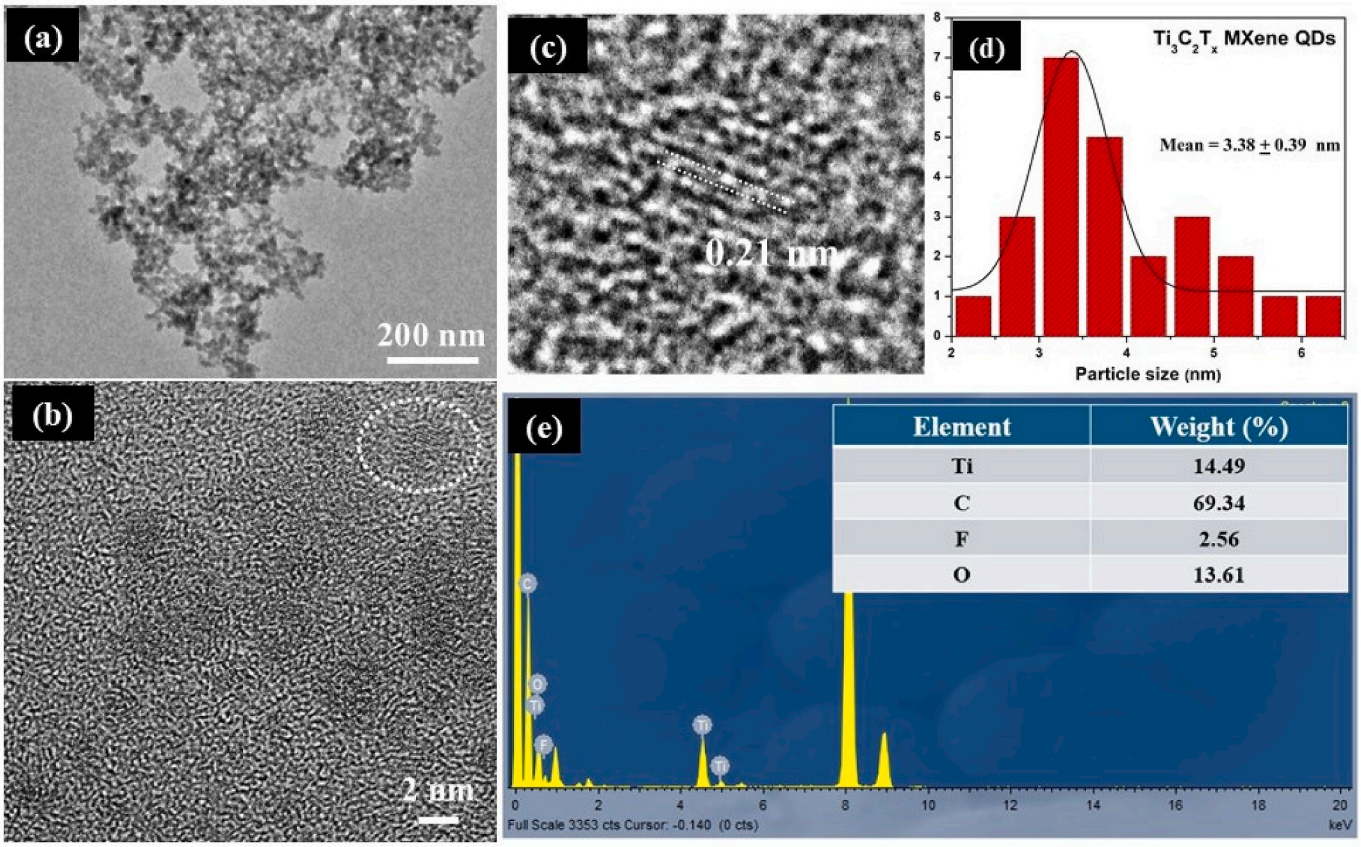



**Fig. 3.** (a) TEM image, (b,c) high-resolution TEM image, (d) size distribution histograms, and (e) EDX of $Ti_3C_2T_x$ MXene QDs.

modification of the carbide environment during the quantum-dot preparation process. Fig. 4c shows two peaks centered at 459.0 (Ti $2p_{3/2}$) and 464.7 eV (Ti $2p_{1/2}$) with a spin–orbit splitting of approximately 5.7 eV [21]. These peaks are assigned to $Ti^{4+}$ species associated predominantly with Ti-O/$TiO_2$. In Fig. 4d, the O 1s peaks located at 530.1, 531.2, 532.0, 533.3, and 534.7 eV are assigned to Ti-O, adsorbed oxygen, C-O-(OH), Ti-$H_2O$, and O-F bonds, respectively [42,44–48]. The pronounced Ti-O contribution further supports the presence of oxidized Ti species in the obtained QDs. Together with the dominant $Ti^{4+}$ components in the Ti 2p spectrum and the absence of a clearly resolved carbide-related C 1s component at low binding energies, these results suggest substantial oxidation of the $Ti_3C_2T_x$ MXene QDs during the $HNO_3$-assisted treatment. In Fig. 4e, the F 1s core-level spectrum exhibits a distinct peak at 685.1 eV, which is attributed to Ti-F-containing surface species originating from the fluorinated surface terminations of the MXene precursor [21,48,49]. For clarity and consistency, the $HNO_3$-treated quantum dots are hereafter referred to as $Ti_3C_2T_x$ MXene QDs to indicate their origin from the $Ti_3C_2T_x$ MXene precursor. However, XPS analysis indicates that the obtained QDs are substantially oxidized and contain Ti-O-rich species. Therefore, the term of $Ti_3C_2T_x$ MXene QDs is used to indicate their $Ti_3C_2T_x$ MXene origin rather than to imply a fully intact carbide structure. Based on the XPS results, which indicate the coexistence of O-, OH–, and F-containing surface species, three idealized $Ti_3C_2T_x$ surface models with O-, OH–, and F-terminations were employed in the DFT calculations to investigate the termination-dependent interaction with water molecules as discussed in the following section. These models are intended to provide mechanistic insight into the role of individual surface functionalities rather than to reproduce the complete atomic structure of the experimentally obtained $HNO_3$-treated QDs, which exhibit substantial oxidation and Ti-O-rich species.

### 3.2. Humidity sensing properties

The fabricated $Ti_3C_2T_x$ MXene QDs humidity sensors were evaluated under RH levels ranging from 10% to 95% RH for eight consecutive cycles as shown in Fig. 5. The results clearly demonstrate that the resistance of the sensors decreases significantly at higher humidity levels and recovers to its initial value when the humidity is reduced to 10% RH. This behavior suggests electron-dominated conduction behavior [50], where the adsorption of electron-donating water molecules on the surface of the $Ti_3C_2T_x$ MXene QDs at high humidity (95% RH) increases the electron carrier concentration, thereby reducing the resistance. The average response is 85.44%. After eight cycles, the response remains approximately 96.09% of its initial value. Although a slight variation in the minimum resistance is observed during the later cycles, the sensor maintains good overall repeatability. In addition, to exclude possible contributions from residual $HNO_3$/NaOH-derived ionic species, a blank sample was prepared using the same chemical treatment and purification procedures but without the $Ti_3C_2T_x$ MXene precursor. The resistance of the blank-treated sensor exceeds the measurable range of the instrument, indicating the absence of a measurable conductive pathway between the electrodes. Furthermore, no detectable electrical response was observed over the relative humidity range of 10–95% RH. These results demonstrate that the $HNO_3$/NaOH-derived residual species alone cannot account for the observed humidity response and support the conclusion that the sensing behavior originates predominantly from the $Ti_3C_2T_x$ MXene-derived material and its humidity-sensitive surface functionalities chemicals. To compare humidity-sensing performance of the $Ti_3C_2T_x$ MXene nanosheets and $Ti_3C_2T_x$ MXene QDs, the resistance responses of both humidity sensors were investigated over a RH range of 10–95% RH as shown in Fig. S2 of Supporting Information. It can be clearly seen that the change in resistance of the $Ti_3C_2T_x$ MXene QDs sensor is significantly greater than that of the $Ti_3C_2T_x$ MXene sensor.

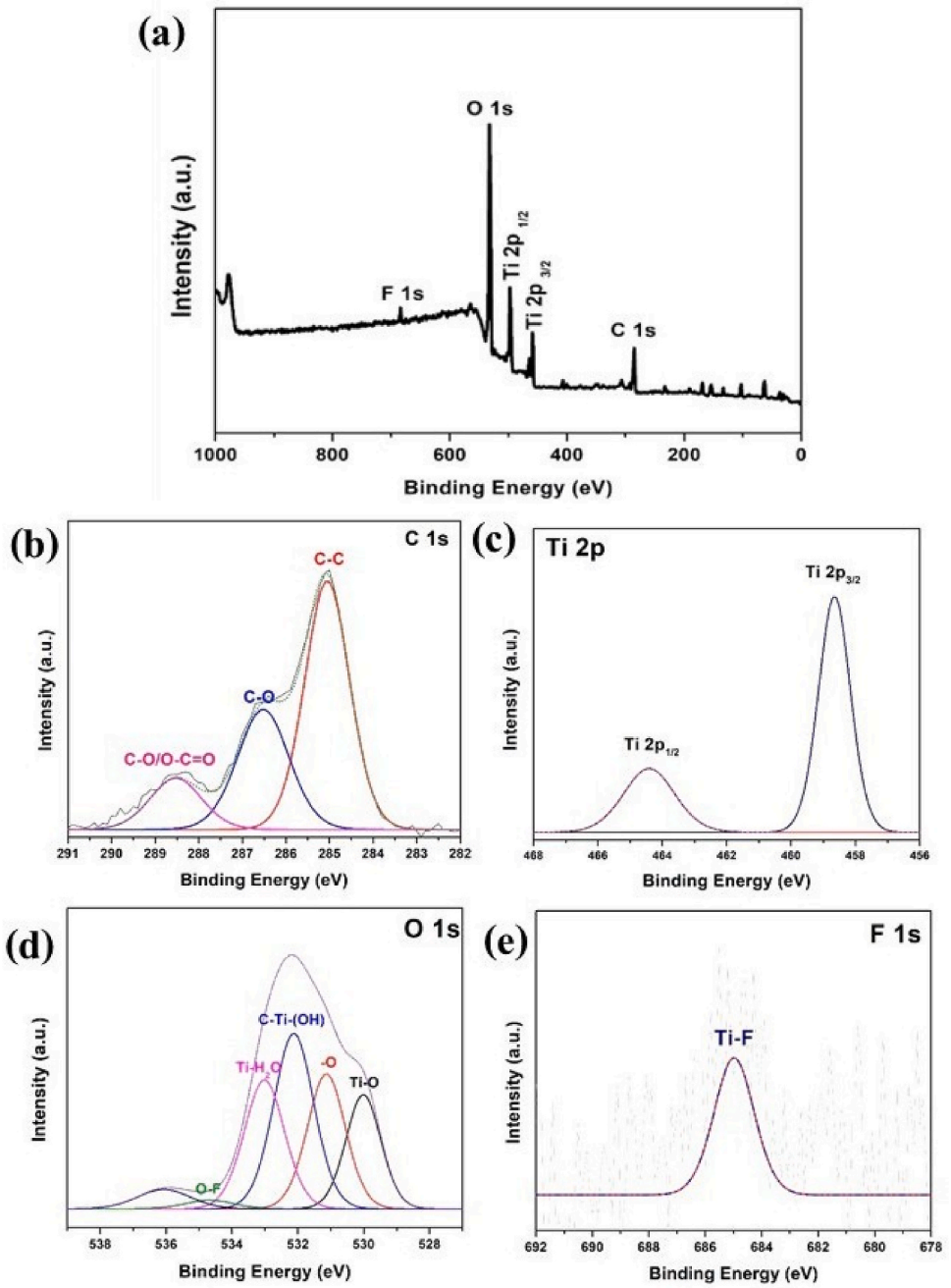



**Fig. 4.** XPS spectra of $Ti_3C_2T_x$ MXene QDs: (a) full survey scan, (b) C 1s, (c) Ti 2p, (d) O 1s, and (e) F 1s.

Interestingly, the $Ti_3C_2T_x$ MXene shows an increase in resistance with increasing RH, whereas the resistance of the $Ti_3C_2T_x$ MXene QDs decrease clearly. For layered $Ti_3C_2T_x$ MXene, water intercalation can expand the interlayer spacing and hinder interflake electron transport, leading to increased resistance [29,50]. In contrast, $Ti_3C_2T_x$ MXene QDs possess a high surface-to-volume ratio and abundant exposed edge-active sites [22], which favor direct $H_2O$ adsorption. At high RH, multilayer water adsorption can assist the formation of continuous hydrogen-bonded water networks, providing additional ionic conduction pathways through a Grotthuss-type proton-hopping mechanism [26]. Consequently, enhanced proton transport contributes to a decrease in sensor resistance with increasing RH. These findings suggest that reducing 2D $Ti_3C_2T_x$ MXene to the quantum-dot scale alters its humidity-dependent charge-transport behavior. However, differences in surface chemistry, oxidation state, and film morphology may also contribute to the observed responses. The sensitivity of the sensor is defined as the slope of the calibration curve obtained from the relationship between sensor resistance and relative humidity (RH) as $Sensitivity = \Delta R/\Delta RH$, where $\Delta R$ and $\Delta RH$ represent the changes in resistance and relative humidity, respectively. The average resistance of the $Ti_3C_2T_x$ MXene QDs humidity sensor decreases from 25.6 MΩ to 2.7 MΩ as the relative humidity increases from 10% to 95% RH, resulting in a sensitivity of 269.4 kΩ/% RH. Fig. 5b presents the response and recovery times of the $Ti_3C_2T_x$ MXene QDs humidity sensor, evaluated from its dynamic resistance changes from 10% RH to 95% RH. It can be observed that the fabricated $Ti_3C_2T_x$ MXene QDs humidity sensor exhibits a short response and recovery times of 35 s and 28 s, respectively, demonstrating excellent humidity sensing performance. The long-term stability of the $Ti_3C_2T_x$ MXene QDs humidity sensor was evaluated over four weeks as shown in Fig. 5c-d. After each weekly measurement,

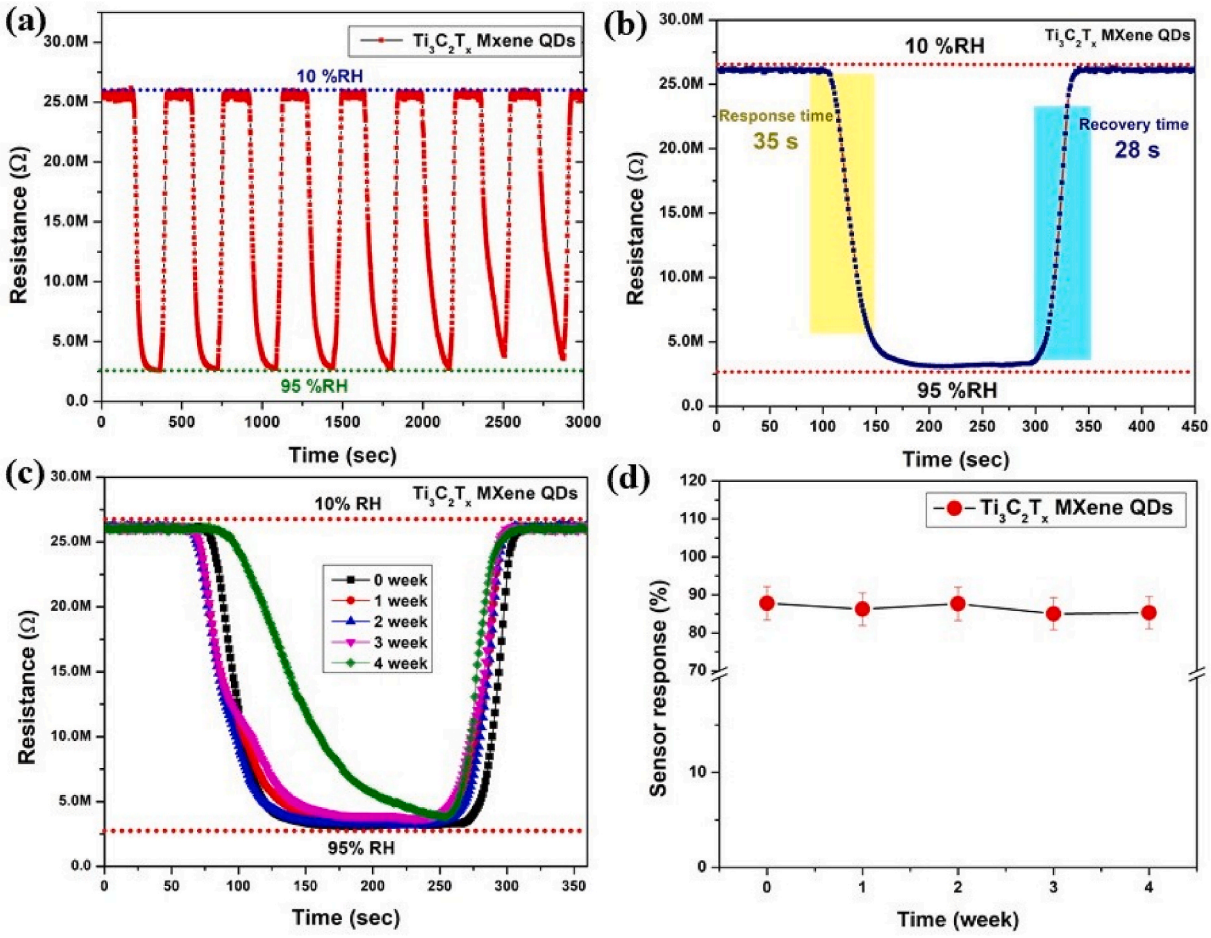



**Fig. 5.** The humidity sensing performance of the $Ti_3C_2T_x$ MXene QD humidity sensor: (a) Changes in resistance of humidity sensor in the relative humidity range of 10–95% RH, (b) response and recovery times, (c) resistance variation and (d) long-term stability performance over 4 weeks in the relative humidity range of 10–95% RH.

the sensor was stored in ambient laboratory conditions at room temperature without controlling humidity and temperature to evaluate its environmental stability. The $Ti_3C_2T_x$ MXene QDs humidity sensors exhibit good long-term stability, showing only a minor decrease in the sensor response from 87.9% to 85.0% after 4 weeks. In comparison with previously reported humidity sensors, the $Ti_3C_2T_x$ MXene QDs humidity sensor developed in this work exhibits competitive sensing performance over a broad RH range as summarized in Table 1.

Compared with the reported humidity sensors summarized in Table 1 [50–67], the $Ti_3C_2T_x$ MXene QDs sensor does not exhibit the best performance in every individual parameter. However, it provides a well-balanced overall sensing performance. The sensor operates over a broad RH range of 10–95%, which is wider than those reported for several resistive sensors [52,55,56,59,61,62]. Its resistance sensitivity of 269.4 kΩ/%RH is also higher than that of several resistance-based sensors [52,53,56,60–62]. In addition, the recovery time of 28 s is shorter than those reported for several MXene- and metal-oxide-based sensors [50,51,55,57,59,61]. Although borophene-based sensors exhibit much higher normalized responses and faster response/recovery times, their response definitions differ from the resistance-based sensitivity used in this work. Overall, the present humidity sensor demonstrates a competitive combination of broad detection range, sensitivity, and reversible response/recovery characteristics.

Fig. 6 presents the hysteresis characteristics of the $Ti_3C_2T_x$ MXene QDs humidity sensor. The sensor was evaluated during humidity adsorption from 10% to 95% RH and desorption from 95% to 10% RH, as shown in Fig. 6a. It can be observed that the resistance of the humidity sensor decreases during humidity adsorption and returns to its baseline value during humidity desorption. Fig. 6b illustrates the sensor response of the $Ti_3C_2T_x$ MXene QDs humidity sensor under humidity adsorption and desorption conditions. The sensor responses for humidity absorption from 10% to 95% RH are 22.5%, 41.6%, 54.9%, 68.6% and 86.1%. Additionally, the sensor responses for humidity desorption from 95% to 10% RH are 86.1%, 68.1%, 55.5%, 41.3% and 23.4%. Humidity hysteresis is defined as the difference between the sensor resistance values measured during the adsorption and desorption processes at the same RH level as shown in Fig. S3 of Supporting Information. The hysteresis error was calculated as $H = |R_{ads} - R_{des}|/S$ [68], where $R_{ads}$ and $R_{des}$ are the resistance values measured during the adsorption and desorption processes, respectively, and S is the sensitivity of the sensor. According to the results, the humidity hysteresis values are calculated to be 0.04% RH, 0.86% RH, 0.32% RH, 0.64% RH, and 0.43% RH at relative humidity of 10, 25, 45, 65, and 85% RH, respectively. The sensor exhibits a maximum hysteresis of approximately 0.86% RH at 25% RH, demonstrating good reversibility between the adsorption and desorption processes over the investigated humidity range.

To investigate the effect of operating temperature on the humidity-sensing performance, the $Ti_3C_2T_x$ MXene QDs sensor was evaluated at room temperature, 35, 45, 55, and 65 °C. As shown in Fig. S4 of Supporting Information, the sensor exhibits pronounced and reversible resistance changes over the relative humidity range of 10–95% RH at room temperature and 35 °C. At 45 °C, the magnitude of the humidity-induced resistance change decreases substantially, whereas no measurable resistance changes were observed at 55 and 65 °C. The reduction in

**Table 1**
Comparison of the performance of various previously reported humidity sensors with the $Ti_3C_2T_x$ MXene QDs humidity sensor developed in this work.

| Sensing material (Sensing type) | RH range (%) | Response | Sensitivity | Res./ Rec. Time (s) | Ref. |
|---|---|---|---|---|---|
| $Ti_3C_2T_x/K_2Ti_4O_9$ (Resistive) | 11–95 | 1.49 [g] | NA | 65.2/ 84.8 | [50] |
| Alkalized $Ti_3C_2T_x$ MXene (Resistive) | 11–95 | ~300 [g] | NA | 1/201 | [51] |
| rGO-SDS composite film (Resistive) | 25–95 | NA | 0.0114 kΩ/ %RH [a] | NA | [52] |
| $SnO_2$/MCM-48 (Resistive) | 11–98 | NA | 0.693 kΩ/ % RH [b] | 9/12 | [53] |
| $CsPbBr_3$ (Impedance) | 11–95 | 72.3% at 67% RH [c] | 1.5565%/ % RH [b] (11–67% RH) | 2.8/9.7 | [54] |
| Perylene (Impedimetric) | 30–90 | NA | −5.289 kΩ/% RH [d] | 120/ 120 | [55] |
| $MoS_2$/PEO (Resistive) | 0–80 | NA | 85 kΩ/% RH [b] | 0.6/0.3 | [56] |
| $SnO_2$ nanoparticles (Resistive) | 11–95 | NA | 1.34 kΩ/% RH [b] (11–75% RH) | 84/576 | [57] |
| $SnO_2$/FDU-12 (Resistive) | 11–98 | NA | 0.574 kΩ/ % RH [b] | 10/14 | [58] |
| MXene/PP (Resistive) | 11–94 | 49.87% [e] | 0.601%/% RH [f] | 17/37 | [59] |
| ZnO/Graphene Foam (Impedance) | 20–95 | NA | 0.033 kΩ/ % RH [b] | NA | [60] |
| MHMA@$Ti_3C_2$ (Resistive) | 30–90 | NA | 63.7 kΩ/% RH [b] | 30/35 | [61] |
| $Ti_3C_2T$/ polyelectrolyte (Resistive) | 10–70 | NA | 0.0016 kΩ/ % RH [b] | 0.11/ 0.22 | [62] |
| Borophene glass (Resistive) | 11–97 | $1.83 \times 10^5$% [e] | NA | 28.8/ 2.6 | [63] |
| $\beta_{12}$-borophene (Resistive) | 11–97 | $3.38 \times 10^7$% [e] | NA | 2.79/ 2.64 | [64] |
| Borophene/$BC_2N$ QDs (Resistive) | 11–97 | 22,001% [e] | NA | 11.82/ 1.41 | [65] |
| Borophene/ graphene (Resistive) | 0–85 | 4,200% [e] | NA | 10.5/ 8.3 | [66] |
| Borophene/$MoS_2$ (Resistive) | 0–97 | 15,500% [e] | NA | 2.5/3.1 | [67] |
| $Ti_3C_2T_x$ MXene QDs (Resistive) | 10–95 | 85.44 [h] | 269.4 kΩ/ % RH [b] | 35/28 | This Work |

Notes: NA: not reported. [a] Sensitivity obtained from the slope of the resistance-RH calibration curve (ΔR/ΔRH). [b] Sensitivity defined as ΔR/ΔRH. [c] Response = $(Z_0\text{-}Z_{RH})/Z_0 \times 100\%$. [d] Sensitivity based on the change in impedance magnitude with RH. [e] Normalized current response, $\Delta I/I_0 \times 100\%$. [f] Sensitivity = Response/ΔRH. [g] Response = $R_{RH}/R_{11\%}$. [h] Response = $(R_0 - R_{RH})/R_0 \times 100\%$, where $R_0$ is the resistance at 10% RH.

humidity response at elevated temperatures is therefore attributed to thermally enhanced desorption and dehydration of weakly bound water molecules from the $Ti_3C_2T_x$ MXene surface. Previous studies have shown that the electrical properties of $Ti_3C_2T_x$ MXene were strongly influenced by water adsorption/desorption and that dehydration can substantially alter its electrical transport behavior [69,70]. Consequently, increased temperature reduces the equilibrium surface water coverage and limits the formation of continuous water-mediated conduction pathways, resulting in the markedly suppressed humidity response observed at 45–65 °C. These results demonstrate that the humidity-sensing characteristics of the $Ti_3C_2T_x$ MXene QDs are strongly dependent on operating temperature.

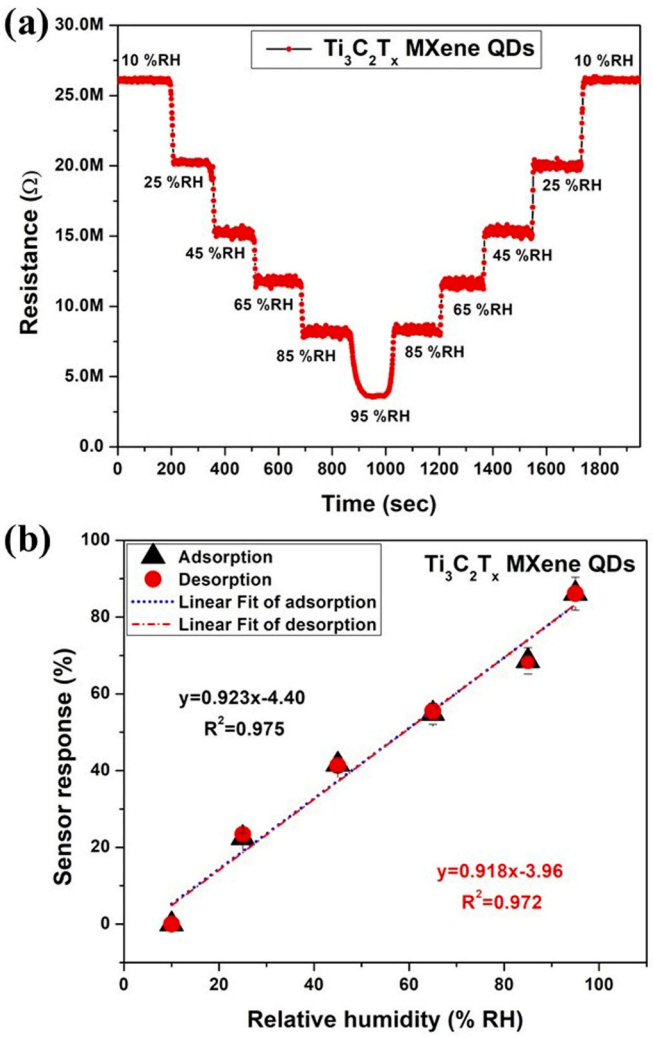



**Fig. 6.** (a) Dynamic resistance response during adsorption (10–95% RH) and desorption (95–10% RH) cycles, and (b) calibration curve of the $Ti_3C_2T_x$ MXene QDs humidity sensor.

### 3.3. Humidity sensing mechanism

The humidity sensing mechanism of the $Ti_3C_2T_x$ MXene QDs is associated with resistance changes induced by the adsorption and desorption of water molecules on the sensor surface. The $Ti_3C_2T_x$ MXene QDs exhibit metal-like conductivity with electron transport dominance with electrons serving as the primary charge carriers [27,51,71,72]. Under humidity conditions, water molecules adsorb onto the surface of the $Ti_3C_2T_x$ MXene QDs and interact with the surface termination groups (−O, −F, −OH) as well as pre-adsorbed oxygen species as shown in Fig. 7a. These interactions promote charge transfer processes, thereby modulating the electron density of the $Ti_3C_2T_x$ MXene QDs. The adsorption of electron-donating water molecules may also facilitate the desorption of pre-adsorbed oxygen species, releasing electrons back into the $Ti_3C_2T_x$ MXene QDs. This process can increase the electron concentration and contribute to the observed decrease in electrical resistance with increasing RH.

In addition, the decrease in the resistance of $Ti_3C_2T_x$ MXene QDs with increasing humidity can be attributed to the Grotthuss chain reaction mechanism [73,74] as presented in Fig. 7b. At low humidity, water molecules form double hydrogen-bonded chemisorption on the surface of $Ti_3C_2T_x$ MXene QDs. As the humidity increases, additional water molecules accumulate on the surface and undergo physical adsorption onto the pre-adsorbed chemisorbed layer, leading to the

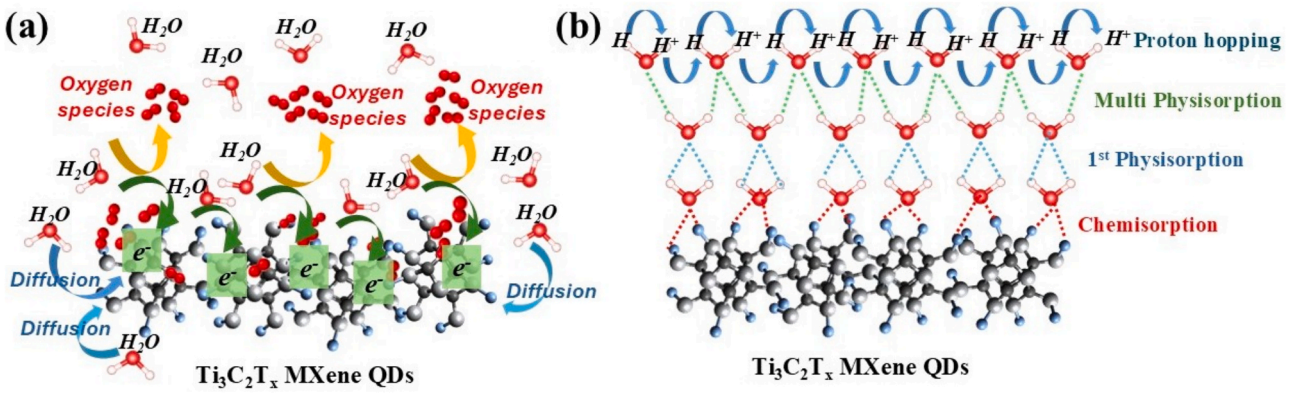



**Fig. 7.** Schematic diagram of (a) the humidity sensing mechanism and (b) the Grotthuss chain reaction mechanism of $Ti_3C_2T_x$ MXene QDs.

formation of multilayer physisorbed water films. Under these conditions, the dominant conduction mechanism gradually shifts from electronic transport to ionic conduction. Protons are transported via a hopping mechanism, contributing to ionic conductivity. In the presence of a continuous hydrogen-bonded network, proton transport occurs through the Grotthuss chain reaction mechanism. Rather than the physical diffusion of hydronium ions ($H_3O^+$), charge transfer proceeds through successive proton hopping between adjacent water molecules, described by the following equation: [26,75] $H_2O + H^+ \rightarrow H_3O^+$ and $H_2O + H_3O^+ \rightarrow H_3O^+ + H_2O$. This mechanism enables rapid proton transfer across the adsorbed water layer, thereby significantly enhancing ionic conductivity. Consequently, the $Ti_3C_2T_x$ MXene QDs humidity sensor exhibits a pronounced reduction in resistance at high RH.

To clarify the humidity-sensing mechanism of the $Ti_3C_2T_x$ MXene QDs humidity sensor, EIS measurements were performed at different RH levels and the corresponding Nyquist plots are shown in Fig. S5 of Supporting Information. At low humidity (25% RH), the Nyquist plot exhibits an incomplete semicircle, which is attributed to the limited ionic conductivity resulting from the small amount of adsorbed water [76]. Under these conditions, charge transport may be predominantly governed by intrinsic electronic conduction within the sensing layer. The corresponding equivalent circuit (EC) can be represented by a resistance ($R_{ct}$) in parallel with a capacitor (C), which approximates a simple parallel RC circuit (insert in Fig. S5(a) of Supporting Information) [77]. At higher humidity (65%, 85% and 95% RH), a low-frequency linear tail appears at the end of the semicircle in the Nyquist plots (Fig. S5(b) of Supporting Information). This feature is associated with Warburg impedance ($Z_W$), indicating an increasing contribution from ionic diffusion through the adsorbed water layer. As the RH increases, additional physically adsorbed water molecules form increasingly interconnected hydrogen-bonded networks on the sensor surface, which are consistent with facilitated proton transport via a Grotthuss-type hopping mechanism [26,77]. Accordingly, the Nyquist plots at high RH can be fitted using an EC consisting of a parallel resistor–capacitor branch together with a Warburg impedance ($Z_W$) connected in series, as shown in the inset of Fig. S5(b) of Supporting Information.

### 3.4. Humidity adsorption on $Ti_3C_2T_x$ MXene QDs based on DFT

To provide a more realistic description of the experimentally observed mixed surface chemistry, $H_2O$ adsorption was further investigated on pristine and defective $Ti_3C_2X_2$ surfaces, where X = F, O, and OH. The calculated adsorption energies and Bader charge transfers are summarized in Table 2. For the ideal fully terminated surfaces, $Ti_3C_2F_2$ and $Ti_3C_2O_2$ exhibit relatively weak $H_2O$ adsorption, with adsorption energies of −0.189 and −0.214 eV, respectively. In comparison, $Ti_3C_2(OH)_2$ shows moderately stronger adsorption, with $E_{ads}$ = -0.471 eV. This difference indicates that the nature of the surface termination itself influences the interaction with water.

**Table 2**
Calculated $H_2O$ adsorption energy ($E_{ads}$), and Bader charge transfer ($\Delta Q$) for pristine and termination-vacancy $Ti_3C_2X_2$ surfaces (X = F, O, and OH).

| | $E_{ads}$ (eV) | $\Delta Q(e)$ |
|---|---|---|
| $Ti_3C_2F_2$ | –0.189 | –0.025 |
| $Ti_3C_2O_2$ | –0.214 | –0.051 |
| $Ti_3C_2O_2H_2$ | –0.471 | –0.086 |
| $Ti_3C_2F_2$-$V_F$ | –0.757 | –0.068 |
| $Ti_3C_2O_2$-$V_O$ | –1.270 | –0.069 |
| $Ti_3C_2(OH)_2$-$V_{OH}$ | –0.790 | –0.433 |

Because the experimentally synthesized $Ti_3C_2X_2$ QDs exhibit mixed F-, O-, and OH-containing surface chemistry rather than an ideal fully terminated surface, termination-deficient local environments were also considered as representative defect sites for $H_2O$ adsorption. A markedly different behavior is observed after introducing termination vacancies. The adsorption energies increase in magnitude to −0.757, −1.270, and −0.790 eV for $Ti_3C_2F_2$-$V_F$, $Ti_3C_2O_2$-$V_O$, and $Ti_3C_2(OH)_2$-$V_{OH}$, respectively. Thus, removal of a surface termination creates under-coordinated sites that interact much more strongly with $H_2O$ than the corresponding fully terminated surfaces. Among the systems considered, the O-vacancy surface exhibits the strongest adsorption.

The Bader charge-transfer results provide further evidence for termination-dependent interactions. The charge transfer for pristine $Ti_3C_2F_2$, $Ti_3C_2O_2$, and $Ti_3C_2(OH)_2$ is −0.025e, −0.051e, and −0.086e, respectively. For the defective surfaces, the corresponding values are −0.068e, −0.069e, and −0.433e. In particular, the substantially larger charge transfer associated with the OH-vacancy system indicates strong electronic coupling between the adsorbed $H_2O$ molecule and the exposed surface site.

Overall, these results indicate that the experimentally observed humidity response cannot be attributed solely to F-vacancies. Instead, the mixed F-, O-, and OH-containing surface chemistry of $Ti_3C_2T_x$ QDs, together with incomplete surface termination, can provide a range of favorable adsorption sites for water molecules. The calculations therefore support a defect-assisted water adsorption mechanism involving multiple types of local surface environments. The present periodic monolayer models are intended to represent these local adsorption environments rather than the complete finite quantum-dot structure, for which edge effects, termination disorder, and finite-size effects may also contribute.

Further insight into the interaction between $H_2O$ and the defective surfaces is provided by the charge-density-difference plots in Fig. 8. Pronounced charge redistribution is observed around the adsorbed $H_2O$ molecule for all three termination-vacancy systems, confirming appreciable electronic interaction between $H_2O$ and the exposed defect sites.

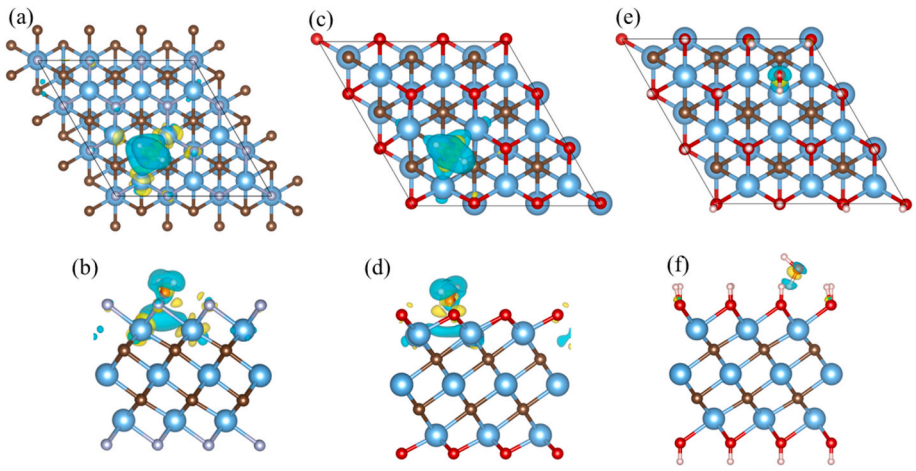



**Fig. 8.** Charge-density-difference isosurfaces for $H_2O$ adsorption on termination-defective $Ti_3C_2X_2$ surfaces: (a,b) $Ti_3C_2F_2$-$V_F$, (c,d) $Ti_3C_2O_2$-$V_O$, and (e,f) $Ti_3C_2(OH)_2$-$V_{OH}$, shown in top and side views, respectively. Yellow and cyan isosurfaces represent charge accumulation and charge depletion upon $H_2O$ adsorption, respectively.

The spatial distribution of charge accumulation and depletion varies with the surface termination, indicating that the local chemical environment strongly influences the interaction with water. In particular, the substantial charge redistribution observed for the OH-vacancy system is consistent with its relatively large Bader charge transfer. For comparison, charge-density-difference plots for $H_2O$ adsorption on the corresponding fully terminated surfaces are provided in Fig. S6 of Supporting Information, where weaker charge redistribution is generally observed.

To further examine the ability of the defective surfaces to accommodate water at increasing coverage, sequential adsorption of up to three $H_2O$ molecules was also considered. Multiple $H_2O$ molecules remain energetically favorably adsorbed on the F-, O-, and OH-vacancy surfaces. In particular, the average adsorption energy on the F-vacancy surface remains approximately −0.75 to −0.80 eV as the number of $H_2O$ molecules increases from one to three. The optimized configurations also show hydrogen bonding between neighboring adsorbed water molecules. These results indicate that termination vacancies can promote the accumulation of water molecules and the formation of hydrogen-bonded clusters. Such water networks are a prerequisite for proton transport at high humidity. Nevertheless, the present calculations do not explicitly describe an extended multilayer water film or proton-hopping barriers, and therefore should not be interpreted as direct theoretical evidence of the Grotthuss mechanism. The average adsorption energies per $H_2O$ molecule for adsorption of 1–3 $H_2O$ molecules on $Ti_3C_2X_2$-$V_x$ are listed in Table S1 of Supporting Information. The atomic configuration of three $H_2O$ molecules adsorbed on $Ti_3C_2F_2$-$V_F$ is also shown in Fig. S7 of Supporting Information.

Overall, the DFT results demonstrate that the interaction of $H_2O$ with $Ti_3C_2T_x$ depends strongly on both the surface termination and the presence of termination vacancies. While the fully F- and O-terminated surfaces exhibit relatively weak $H_2O$ adsorption, removal of F, O, or OH terminations substantially strengthens the adsorption. These findings indicate that the experimentally observed humidity response should not be attributed exclusively to F-vacancies. Instead, the mixed F-, O-, and OH-containing surface chemistry, together with incomplete surface termination, can provide multiple favorable adsorption sites for water molecules. The periodic monolayer models used here represent local adsorption environments rather than the complete $Ti_3C_2T_x$ QD structure. Therefore, finite-size effects, edge sites, termination disorder, and interactions under realistic humid conditions are not explicitly included in the present calculations.

## 4. Conclusion

In summary, $Ti_3C_2T_x$ MXene QDs were successfully synthesized via a top-down solvothermal approach and employed as an efficient resistive-type humidity sensor. Structural and compositional characterizations (XRD, XPS, and HRTEM) confirmed the successful formation of ultrasmall $Ti_3C_2T_x$ MXene QDs with mixed surface terminations and an average size of approximately 3.4 nm. The fabricated sensor exhibited excellent humidity sensing performance over a wide range of 10–95% RH including high response (85.44%), high sensitivity (269.4 kΩ/%RH), fast response/recovery times (35/28 s), low hysteresis (< 0.86%), good repeatability, and stable operation over four weeks. The sensing mechanism is attributed to the synergistic contribution of electronic and ionic processes. Specifically, water adsorption on surface functional groups modulates the electron density of $Ti_3C_2T_x$ MXene QDs, while proton transport through hydrogen-bonded networks via the Grotthuss chain reaction dominates at high humidity, leading to a significant reduction in resistance. The DFT calculations provide deeper insight into the role of surface chemistry, showing distinct $H_2O$ adsorption behaviors on O-, OH–, and F-terminated $Ti_3C_2T_x$ surfaces, with the corresponding termination vacancies generally enhancing adsorption strength and charge transfer relative to vacancy-free surfaces. These defect sites act as dominant active centers for water adsorption and are crucial for achieving high sensing performance. The theoretical results are consistent with experimental observations and highlight the importance of defect-induced adsorption in governing sensor response. This study demonstrates that defect-engineered $Ti_3C_2T_x$ MXene QDs are highly promising materials for advanced humidity sensing applications and provides a comprehensive understanding of the structure–property relationship through combined experimental and theoretical approaches.

## CRediT authorship contribution statement

**Yotsarayuth Seekaew:** Writing – original draft, Visualization, Methodology, Investigation, Formal analysis, Data curation, Conceptualization. **Weeraphat Pon-On:** Investigation. **Pakpoom Reunchan:** Writing – original draft, Methodology, Investigation, Formal analysis. **Audomsak Sripothongnack:** Methodology, Investigation. **Chatchawal Wongchoosuk:** Writing – review & editing, Validation, Supervision, Software, Resources, Funding acquisition, Formal analysis, Conceptualization.

## Declaration of competing interest

The authors declare that they have no known competing financial interests or personal relationships that could have appeared to influence the work reported in this paper.

## Acknowledgments

This project is funded by National Research Council of Thailand (NRCT) and Kasetsart University Research and Development Institute (KURDI), Kasetsart University under the grant number of N42A690366. Y.S. acknowledges Ramkhamhaeng University for any supports of this work.

## Appendix A. Supplementary data

Supplementary data to this article can be found online at https://doi.org/10.1016/j.apsusc.2026.168810.

## Data availability

Data will be made available on request.

## References

[1] Q. Wang, Z. Duan, D. Liu, Z. Yuan, Y. Jiang, H. Tai, Recent advances in flexible paper-based humidity sensors: fabrication, mechanisms, performances, and applications, Nanoscale Horiz. 11 (7) (2026) 1801–1822.
[2] M. Zhang, Z. Duan, Z. Yuan, Y. Jiang, H. Tai, Observing mixed chemical reactions at the positive electrode in the high-performance self-powered electrochemical humidity sensor, ACS Nano 18 (50) (2024) 34158–34170.
[3] J. Hu, Z. Duan, C. Tan, Y. Wang, Z. Yuan, Y. Jiang, H. Tai, Self-powered electrochemical humidity sensor based on Cu/(cellulose nanocrystals/NaCl)/Zn structure for respiratory rate detection, Inorg. Chem. Commun. 180 (2025) 114994.
[4] X. Leng, C. Wang, Z. Duan, Y. Wang, Q. Wang, Z. Yuan, Y. Jiang, H. Tai, Electrochemical humidity sensors based on LiCl/carbon ink with adjustable humidity sensing and enhanced power generation performances, Sens. Actuators B Chem. 464 (2026) 140140.
[5] C. Tan, Z. Duan, M. Zhang, Y. Wu, Z. Yuan, Y. Jiang, H. Tai, Proton conduction of polyaniline for electrochemical humidity sensor, Sens. Actuators B Chem. 446 (2026) 138661.
[6] H. Yang, W. Wang, D. Tang, C. Tan, Z. Duan, Y. Wang, Z. Yuan, Y. Jiang, H. Tai, High-performance electrochemical humidity sensor based on [BMIM]$BF_4$ ionic liquid with wide detection range, low detection limit and high detection resolution, Mater. Today Chem. 54 (2026) 103711.
[7] B. Anasori, M.R. Lukatskaya, Y. Gogotsi, 2D metal carbides and nitrides (MXenes) for energy storage, Nat. Rev. Mater. 2 (2) (2017) 16098.
[8] Y. Gogotsi, B. Anasori, The rise of MXenes, ACS Nano 13 (8) (2019) 8491–8494.
[9] X. Guo, Y. Ding, D. Kuang, Z. Wu, X. Sun, B. Du, B. Liang, Y. Wu, W. Qu, L. Xiong, Y. He, Enhanced ammonia sensing performance based on MXene-$Ti_3C_2T_x$ multilayer nanoflakes functionalized by tungsten trioxide nanoparticles, J. Colloid Interface Sci. 595 (2021) 6–14.
[10] H.V. Neelamana, S.M. Rekha, S.V. Bhat, $Ti_3C_2T_x$ MXene: a new promising 2D material for optoelectronics, Chem. Mater. 35 (18) (2023) 7386–7405.
[11] Y. Seekaew, S. Kamlue, C. Wongchoosuk, Room-temperature ammonia gas sensor based on $Ti_3C_2T_x$ MXene/graphene oxide/CuO/ZnO nanocomposite, ACS Appl. Nano Mater. 6 (10) (2023) 9008–9020.
[12] M. Downes, C.E. Shuck, B. McBride, J. Busa, Y. Gogotsi, Comprehensive synthesis of $Ti_3C_2T_x$ from MAX phase to MXene, Nat. Protoc. 19 (2024) 1807–1834.
[13] I.-.-P. Chen, A.A. Kashale, Y.-H. Pan, Hydrofluoric acid-free synthesis of $Ti_3C_2T_x$ MXene nanostructures for energy applications, ACS Appl. Nano Mater. 6 (3) (2023) 1985–1995.
[14] S. Kotteeswaran, S. Kondee, W. Pon-On, W.H. Al-Qahtani, C. Wongchoosuk, M. Govindasamy, CuZnS microflowers anchored on MXene nanosheets based electrochemical sensor for pico-molar determination of chloramphenicol in biological samples and dairy products, Microchem. J. 212 (2025) 113291.
[15] G. Chaloeipote, C. Wongchoosuk, Flexible humidity sensor based on PEDOT:PSS/Mxene nanocomposite, Flex. Print. Electron. 9 (2024) 015015.
[16] R. Rajamanikandan, K. Sasikumar, H. Ju, $Ti_3C_2$ MXene quantum dots as an efficient fluorescent probe for bioflavonoid quercetin quantification in food samples, Anal. Chim. Acta 1322 (2024) 343069.
[17] Q. Xue, H. Zhang, M. Zhu, Z. Pei, H. Li, Z. Wang, Y. Huang, Y. Huang, Q. Deng, J. Zhou, S. Du, Q. Huang, C. Zhi, Photoluminescent $Ti_3C_2$ MXene quantum dots for multicolor cellular imaging, Adv. Mater. 29 (2017) 1604847.
[18] Y. Feng, F. Zhou, Q. Deng, C. Peng, Solvothermal synthesis of in situ nitrogen-doped $Ti_3C_2$ MXene fluorescent quantum dots for selective $Cu2^+$ detection, Ceram. Int. 46 (6) (2020) 8320–8327.
[19] X. Yu, X. Cai, H. Cui, S.-W. Lee, X.-F. Yu, B. Liu, Fluorine-free preparation of titanium carbide MXene quantum dots with high near-infrared photothermal performances for cancer therapy, Nanoscale 9 (2017) 17859–17864.
[20] Z. Feng, G. Yiyu, J. Libin, W. Qiao, MXene quantum dot synthesis, optical properties, and ultra-narrow photonics: a comparison of various sizes and concentrations, Laser Photonics Rev. 15 (2021) 2100059.
[21] F. Yang, Y. Ge, T. Yin, J. Guo, F. Zhang, X. Tang, M. Qiu, W. Liang, N. Xu, C. Wang, Y. Song, S. Xu, S. Xiao, $Ti_3C_2Tx$ MXene quantum dots with enhanced stability for ultrafast photonics, ACS Appl. Nano Mater. 3 (12) (2020) 11850–11860.
[22] C. Guan, X. Yue, J. Fan, Q. Xiang, MXene quantum dots of $Ti_3C_2$: Properties, synthesis, and energy-related applications, Chin. J. Catal. 43 (10) (2022) 2484–2499.
[23] F. Ai, C. Fu, G. Cheng, H. Zhang, Y. Feng, X. Yan, X. Zheng, Amino-functionalized $Ti_3C_2$ MXene quantum dots as photoluminescent sensors for diagnosing histidine in human serum, ACS Appl. Nano Mater. 4 (8) (2021) 8192–8199.
[24] Y. Jiang, L. Wu, Q. Chen, N. Li, J. Tian, High-performance capacitive humidity sensor based on flower-like $SnS_2/Ti_3C_2$ MXene for respiration monitoring and non-contact sensing, Sens. Actuators B Chem. 426 (2025) 137012.
[25] Y. Han, H. Cao, Y. Cao, Y. Yao, Z. Yin, X. Huang, Y. Zhu, Z. Zhu, $ZnS/Ti_3C_2T_x$ MXene nanocomposites based humidity sensor with improved sensing performance, Sens. Actuators B Chem. 433 (2025) 137503.
[26] L. Wang, X. Yao, S. Yuan, Y. Gao, R. Zhang, X. Yu, S.-T. Tu, S. Chen, Ultra-high performance humidity sensor enabled by a self-assembled $CuO/Ti_3C_2T_X$ MXene, RSC Adv. 13 (2023) 6264–6273.
[27] Y. Han, H. Cao, Y. Cao, X. Wen, Y. Yao, Z. Zhu, Fast response flexible humidity sensors based on $Ti_3C_2T_x$ MXene-heterostructures for multifunctional applications, J. Mater. Chem. C 12 (2024) 4809–4816.
[28] T. Liu, D. Qu, L. Guo, G. Zhou, G. Zhang, T. Du, W. Wu, MXene/TPU composite film for humidity sensing and human respiration monitoring, Adv. Sensor Res. 3 (2024) 2300014.
[29] E.S. Muckley, M. Naguib, H.-W. Wang, L. Vlcek, N.C. Osti, R.L. Sacci, X. Sang, R. R. Unocic, Y. Xie, M. Tyagi, E. Mamontov, K.L. Page, P.R.C. Kent, J. Nanda, I. N. Ivanov, Multimodality of structural, electrical, and gravimetric responses of intercalated MXenes to water, ACS Nano 11 (11) (2017) 11118–11126.
[30] S. Célérier, S. Hurand, C. Garnero, S. Morisset, M. Benchakar, A. Habrioux, P. Chartier, V. Mauchamp, N. Findling, B. Lanson, E. Ferrage, Hydration of $Ti_3C_2T_x$ MXene: an Interstratification Process with Major Implications on Physical Properties, Chem. Mater. 31 (2) (2019) 454–461.
[31] M. Huzaifa, M. Shafiq, N. Ali, C. Cocchi, M. N.-e-Alam, Z. Ul-Haq,, Au-decorated $Ti_3C_2$ MXene sensor for enhanced detection of gaseous toxins (CO, $COCl_2$, $H_2S$, $NH_3$, $NO_2$): a DFT study, ACS Omega 10 (1) (2025) 1562–1570.
[32] Y. Peng, Y. Zhao, Y. Yuan, W. Meng, W. Jiang, X. Wang, High-response humidity sensing with graphene oxide/lignosulfonate and laser-induced graphene for respiratory health, RSC Adv. 15 (15) (2025) 11739–11748.
[33] G. Kresse, J. Hafner, Ab initio molecular dynamics for liquid metals, Phys. Rev. B 47 (1993) 558–561.
[34] G. Kresse, J. Furthmüller, Efficiency of ab-initio total energy calculations for metals and semiconductors using a plane-wave basis set, Comput. Mater. Sci 6 (1996) 15–50.
[35] J.P. Perdew, K. Burke, M. Ernzerhof, Generalized gradient approximation made simple, Phys. Rev. Lett. 77 (1996) 3865–3868.
[36] S. Grimme, J. Antony, S. Ehrlich, H. Krieg, A consistent and accurate ab initio parametrization of density functional dispersion correction (DFT-D) for the 94 elements H-Pu, J. Chem. Phys. 132 (2010) 154104.
[37] S. Grimme, S. Ehrlich, L. Goerigk, Effect of the damping function in dispersion corrected density functional theory, J. Comput. Chem. 32 (2011) 1456–1465.
[38] A. Sripothongnack, W. Teeranattapong, A. Ananchuensook, T. Thanasarnsurapong, J. T-Thienprasert, C. Wongchoosuk, P. Reunchan,, Unveiling the role of metal-doped $BNC_2$ monolayer for selective gas adsorption: a DFT investigation, Surf. Interfaces 56 (2025) 105481.
[39] W. Teeranattapong, A. Sripothongnack, T. Thanasarnsurapong, C. Wongchoosuk, P. Reunchan, Tunable gas sensing properties of metal-doped $C_3N$ for agricultural molecule detection: a DFT study, Surf. Interfaces 80 (2026) 108318.
[40] H. Alijani, A.R. Rezk, M.M. Khosravi Farsani, H. Ahmed, J. Halim, P. Reineck, B. J. Murdoch, A. El-Ghazaly, J. Rosen, L.Y. Yeo, Acoustomicrofluidic synthesis of pristine ultrathin $Ti_3C_2T_z$ MXene nanosheets and quantum dots, ACS Nano 15 (2021) 12099–12108.
[41] B.P. Thapaliya, C.J. Jafta, H. Lyu, J. Xia, H.M. Meyer III, M.P. Paranthaman, X.-G. Sun, C.A. Bridges, S. Dai, Fluorination of Mxene by elemental $F_2$ as electrode material for lithium-ion batteries, ChemSusChem 12 (2019) 1316.
[42] J. Gou, L. Zhao, J. Yan Li, Zhang,, Nitrogen-doped $Ti_2C$ MXene quantum dots as antioxidants, ACS Appl. Nano Mater. 4 (2021) 12308–12315.
[43] Z. Dessoliers, A. Chemin, G. Valurouthu, R. Lord, T. Bilyk, Y. Gogotsi, V. Mauchamp, T. Petit, Combining X-Ray photoelectron and absorption spectroscopies for determining surface chemistry and composition of $Ti_3C_2T_x$ MXene, Adv. Mater. Interfaces 12 (2025) 2500391.
[44] G. Xu, Y. Niu, X. Yang, Z. Jin, Y. Wang, Y. Xu, H. Niu, Preparation of $Ti_3C_2Tx$ MXene-derived quantum dots with white/blue-emitting photoluminescence and electrochemiluminescence, Adv. Optical Mater. 6 (2018) 1800951.
[45] Z. Yin, Z. Lu, Y. Xu, Y. Zhang, L. He, P. Li, L. Xiong, L. Ding, Y. Wei, H. Wang, Supported MXene/GO composite membranes with suppressed swelling for metal ion sieving, Membranes 11 (8) (2021) 621.
[46] L. Zhaoa, Z. Wanga, Y. Lia, S. Wanga, L. Wanga, Z. Qia, Q. Gea, X. Liua, J.Z. Zhang, Designed synthesis of chlorine and nitrogen co-doped $Ti_3C_2$ MXene quantum dots and their outstanding hydroxyl radical scavenging properties, J. Mater. Sci. Technol. 78 (2021) 30–37.

[47] W.Y. Chen, X. Jiang, S.-N. Lai, D. Peroulis, L. Stanciu, Nanohybrids of a MXene and transition metal dichalcogenide for selective detection of volatile organic compounds, Nat. Commun. 11 (2020) 1302.
[48] G. Akhlamadi, E.K. Goharshadi, H. Liimatainen, Ultrahigh fluid sorption capacity of superhydrophobic and tough cryogels of crosslinked cellulose nanofibers, cellulose nanocrystals, and $Ti_3C_2T_x$ MXene nanosheets, J. Mater. Chem. A 10 (2022) 24746–24760.
[49] S.A. Shah, T. Habib, H. Gao, P. Gao, W. Sun, M.J. Green, M. Radovic, Template-free 3D titanium carbide ($Ti_3C_2T_x$) MXene particles crumpled by capillary forces, Chem. Commun. 53 (2017) 400–403.
[50] J. Wu, P. Lu, J. Dai, C. Zheng, T. Zhang, W.W. Yu, Y. Zhang, High performance humidity sensing property of $Ti_3C_2T_x$ MXene-derived $Ti_3C_2T_x/K_2Ti_4O_9$ composites, Sens. Actuators B Chem. 326 (2021) 128969.
[51] Z. Yang, A. Liu, C. Wang, F. Liu, J. He, S. Li, J. Wang, R. You, X. Yan, Y. Peng Sun, G.L. Duan, Improvement of gas and humidity sensing properties of organ-like MXene by alkaline treatment, ACS Sensors 4 (5) (2019) 1261–1269.
[52] C. Lei, J. Zhang, T. Liang, R. Liu, Z. Zhao, J. Xiong, K. Yin, Humidity sensor based on rGO-SDS composite film, Micromachines 13 (2022) 504.
[53] P. Malik, S. Duhan, R. Malik, A high-performance humidity sensor based on 3D porous $SnO_2$-encapsulated MCM-48 for real-time breath monitoring and contactless gesture detection, Mater. Adv. 5 (2024) 2510–2525.
[54] Z. Wu, J. Yang, X. Sun, Y. Wu, L. Wang, G. Meng, D. Kuang, X.Z. Guo, W. Qu, B. Du, C. Liang, X. Fang, X. Tang, Y. He, An excellent impedance- type humidity sensor based on halide perovskite $CsPbBr_3$ nanoparticles for human respiration monitoring, Sens. Actuators B Chem. 337 (2021) 129772.
[55] S. Vasquez, S. Morales-Cámara, C. Moraila, Y. Houeix, I.B. Pascual, J.F. Salmerón, A. R.-Diéguez, S. Rojas, N. Münzenrieder, L. Petti, P. Lugli, A. Rivadeneyra,, Enhancing humidity sensing with functionalized perylene-coated dispense printed electrodes: a comparative study, ACS Appl. Electron. Mater. 7 (14) (2025) 6311–6321.
[56] H.M. Zeeshan Yousaf, S.W. Kim, G. Hassan, K. Karimov, K.H. Choi, M. Sajid, Highly sensitive wide range linear integrated temperature compensated humidity sensors fabricated using electrohydrodynamic printing and electrospray deposition, Sens. Actuators B Chem. 308 (2020) 127680.
[57] A. Kumar, P. Kumari, M.S. Kumar, G. Gupta, D.D. Shivagan, K. Bapna, $SnO_2$ nanostructured thin film as humidity sensor and its application in breath monitoring, Ceram. Int. 49 (2023) 24911–24921.
[58] S. Sehrawat, S. Duhan, S.P. Nehra, Low temperature approach towards synthesis and fabrication of resistive humidity sensor elicited from $SnO_2$-modified mesoporous FDU-12, J. Mater. Sci. Mater. Electron. 35 (2024) 999.
[59] T. Liu, Y. Rong, G. Zhou, G. Zhang, C. Su, P. Li, X. Yin, G. Wang, W. Wu, L. Zhang, Direct-writing MXene/polypropylene composites for wearable humidity sensors with multiple applications, IEEE Sens. J. 24 (2024) 15241–15251.
[60] M. Morsy, M. Ibrahim, Z. Yuan, F. Meng, Graphene foam decorated with ZnO as a humidity sensor, IEEE Sens. J. 20 (2020) 1721–1729.
[61] X. Hu, X. Yu, Z. Yu, S. Li, T. Jin, Y. Chen, $Ti_3C_2$-MXene used to enhance response/recovery speed and thermal stability of acrylate copolymer humidity sensor under abnormal temperature changes, Eur. Polym. J. 203 (2024) 112658.
[62] H. An, T. Habib, S. Shah, H. Gao, A. Patel, I. Echols, X. Zhao, M. Radovic, M. J. Green, J.L. Lutkenhaus, Water sorption in MXene/Polyelectrolyte multilayers for ultrafast humidity sensing, ACS Appl. Nano Mater. 2 (2) (2019) 948–955.
[63] Z. Wu, X. Liang, Z. Zhao, Q. Wu, X. Liu, Y. Liu, M. Xu, C. Hou, G. Tai, Ultrasensitive and durable borophene-based humidity sensors for advanced human-centric applications, Chem. Eng. J. 500 (2024) 156881.
[64] R. Zhu, Z. Wu, Z. Zhao, M. Xu, C. Hou, G. Tai, Ultrasensitive $\beta_{12}$-borophene humidity sensor for intelligent humidity interfaces, Chem. Eng. J. 521 (2025) 167088.
[65] X. Liu, C. Hou, Y. Liu, S. Chen, Z. Wu, X. Liang, G. Tai, Borophene and $BC_2N$ quantum dot heterostructures: ultrasensitive humidity sensing and multifunctional applications, J. Mater. Chem. A 11 (45) (2023) 24789–24799.
[66] C. Hou, G. Tai, B. Liu, Z. Wu, Y. Yin, Borophene-graphene heterostructure: Preparation and ultrasensitive humidity sensing, Nano Res. 14 (2021) 2337–2344.
[67] C. Hou, G. Tai, Y. Liu, Z. Wu, Z. Wu, X. Liang, Ultrasensitive humidity sensing and the multifunctional applications of borophene–$MoS_2$ heterostructures, J. Mater. Chem. A 9 (22) (2021) 13100–13108.
[68] Y. Zu, Z. Duan, Z. Yuan, Y. Jiang, H. Tai, Electrospun nanofiber-based humidity sensors: materials, devices, and emerging applications, J. Mater. Chem. A 12 (2024) 27157–27179.
[69] H. Zhang, H. Jiang, Y. Li, W. Wei, F. Wu, M. Qi, Y. Wu, J. Li, C. Deng, Electrical, thermal and thermoelectric properties of $Ti_3C_2T_x$ films: uncovering the significant role of water molecules, J. Mater. Chem. C 11 (47) (2023) 16792–16805.
[70] L. Yu, D. Huang, X. Wang, W. Yu, Y. Yue, Tuning thermal and electrical properties of MXenes via dehydration, Phys. Chem. Chem. Phys. 24 (42) (2022) 25969–25978.
[71] A. Rambabu, D.K. Singh, R. Pant, K.K. Nanda, S.B. Krupanidhi, Self-powered, ultrasensitive, room temperature humidity sensors using $SnS_2$ nanofilms, Sci. Rep. 10 (2020) 14611.
[72] S. Cho, S.H. Lim, J. Oh, T.-S. Ju, S. Yang, H.H. Kim, Y. Kim, Synthesis-in-place of $V_2O_5$ nanobelts for wide range humidity detection, Sens. Actuators B Chem. 423 (2025) 136711.
[73] N. Agmon, The Grotthuss mechanism, Chem. Phys. Lett. 244 (1995) 456–462.
[74] S. Ding, X. Jin, B. Wang, Z. Niu, J. Ma, X. Zhao, M. Yang, C. Wang, Q. Shi, X. Li, Integrating $Ti_3C_2T_x$ MXene nanosheets with thermoplastic polyurethane nanofibers as wearable humidity sensors for noninvasive sleep monitoring and noncontact sensing, ACS Appl. Nano Mater. 6 (13) (2023) 11810–11821.
[75] Z. Zhang, H. Ma, F. Si, Q. Liu, J. Li, L. Tian, J. Ding, W. Zhang, X. Fan, Highly sensitive flexible humidity sensor based on bacterial cellulose/MXene/graphene oxide composite film, ACS Appl. Electron. Mater. 7 (21) (2025) 9946–9954.
[76] N. Li, Y. Jiang, C. Zhou, Y. Xiao, B. Meng, Z. Wang, D. Huang, C. Xing, Z. Peng, High-performance humidity sensor based on urchin-like composite of $Ti_3C_2$ MXene-derived $TiO_2$ nanowires, ACS Appl. Mater. Interfaces 11 (41) (2019) 38116–38125.
[77] F. Liu, J. Hong, X. Chen, X. Ding, S. Li, X. Yu, J. Lu, X. Zhao, K. Tang, C. Xie, K. Zhao, Ultrafast humidity sensor and transient humidity detections in high dynamic environments, Commun. Eng. 4 (2025) 4.